Clay Minerals, (2018) **53**, 579–602

Low-grade evolution of clay minerals and organic matter in fault zones of the Hikurangi prism (New Zealand)

TATIANA MAISON[1,*], SÉBASTIEN POTEL[1], PIERRE MALIÉ[1,2], RAFAEL FERREIRO MÄHLMANN[3], FRANK CHANIER[4], GEOFFROY MAHIEUX[5] AND JULIEN BAILLEUL[1]

[1] *UniLaSalle, UPJV, EA 7511 Basins-Reservoirs-Resources (B2R), F-60026 Beauvais, France*
[2] *Laboratoire Géosciences Université de Montpellier CC, 60 Place E, Bataillon, 34095 Montpellier, Cedex 5, France*
[3] *Technische Universität Darmstadt, Technical and Low Temperature Petrology, Institut für Angewandte Geowissenschaften, 64287 Darmstadt, Germany*
[4] *Univ. Lille, CNRS, Univ. Littoral Côte d'Opale, UMR 8187, LOG, Laboratoire d'Océanologie et de Géosciences, F 59000 Lille, France*
[5] *UPJV, UniLaSalle, EA 7511 Basins-Reservoirs-Resources (B2R), F-80000 Amiens, France*

(*Received 15 November 2017; revised 12 August 2018; Accepted Manuscript published online: 27 November 2018; Version of Record published online: 22 January 2019; Guest Associate Editor: A. Schleicher*)

ABSTRACT: Clay minerals and organic matter occur frequently in fault zones. Their structural characteristics and their textural evolution are driven by several formation processes: (1) reaction by metasomatism from circulating fluids; (2) *in situ* evolution by diagenesis; and (3) neoformation due to deformation catalysis. Clay-mineral chemistry and precipitated solid organic matter may be used as indicators of fluid circulation in fault zones and to determine the maximum temperatures in these zones. In the present study, clay-mineral and organic-matter analyses of two major fault zones – the Adams-Tinui and Whakataki faults, Wairarapa, North Island, New Zealand – were investigated. The two faults analysed correspond to the soles of large imbricated thrust sheets formed during the onset of subduction beneath the North Island of New Zealand. The mineralogy of both fault zones is composed mainly of quartz, feldspars, calcite, chabazite and clay minerals such as illite-muscovite, kaolinite, chlorite and mixed-layer minerals such as chlorite-smectite and illite-smectite. The diagenesis and very-low-grade metamorphism of the sedimentary rock is determined by gradual changes of clay mineral 'crystallinity' (illite, chlorite, kaolinite), the use of a chlorite geothermometer and the reflectance of organic matter. It is concluded here that: (1) the established thermal grade is diagenesis; (2) tectonic strains affect the clay mineral 'crystallinity' in the fault zone; (3) there is a strong correlation between temperature determined by chlorite geothermometry and organic-matter reflectance; and (4) the duration and depth of burial as well as the pore-fluid chemistry are important factors affecting clay-mineral formation.

KEYWORDS: clay minerals, Kübler index, diagenesis, very-low-grade metamorphism, chlorite geothermometry, faults, East Coast Basin, New Zealand.

*E-mail: tatiana.maison@unilasalle.fr
This paper was presented during the session 'GG01: Clays in faults and fractures + MI-03 Clay mineral reaction progress in very low-grade temperature petrologic studies' of the International Clay Conference 2017.
https://doi.org/10.1180/clm.2018.46

Major faults in sedimentary basins modify significantly the potential for fluid migration, mineralization and hydrocarbon production. During the formation, infill and evolution of sedimentary basins, faults adopt burial, pre-, syn- and post-kinematic deformation

patterns that reflect the structural setting and ambient stress field. Consequently, their hydrological and mechanical behaviours change over time. The evolution of faults, and also of sedimentary basins, may be approached by analysis of their physicochemical properties in order to quantify the evolution of thermo-barometric markers. One of these thermo-barometric markers is the 'crystallinity' of clay minerals (*e.g.* illite and chlorite). The present study is based on illite 'crystallinity' (IC). The IC or Kübler index (KI; referring to the pioneering study of Kübler, 1964) is defined as the full width at half maximum (FWHM) of the first illite basal reflection at 10 Å in X-ray diffraction (XRD) patterns, expressed in $\Delta°2\theta$ (Frey, 1987; Guggenheim *et al.*, 2002). Guggenheim *et al.* (2002) recommended that the use of the term 'crystallinity index' should be avoided, although it may be placed within quotation marks when referring to previously referenced work. By combining the study of clay minerals (reaction series of phyllosilicates) and organic matter (vitrinite and solid bitumen reflectance) researchers aim to characterize basin thermal evolution, burial depth, subsidence history, eroded load and the role of clays in fault zones.

The occurrence of major fluid migrations along decollements in subduction wedges is well known and well documented (Le Pichon *et al.*, 1990; Moore *et al.*, 1990, 1995; Moore & Vrolijk, 1992; Lewis & Marshall, 1996; Bangs *et al.*, 1999; Bruhn *et al.*, 2000; Henry *et al.*, 2002; Sibson & Rowland, 2003; Barnes *et al.*, 2010). However, the history of fluid–rock interaction, the composition of migrating fluids and the pathways of fluid circulation are less well understood. Orogenic prisms with active fluid systems are often offshore, and thus models of fluid migration along faults are generally based on marine seismic studies of present-day systems (for the New Zealand eastern margin, see Henrys *et al.*, 2009; Barnes *et al.*, 2010; Crutchley *et al.*, 2010; Pecher *et al.*, 2010; Plaza-Faverola *et al.*, 2012, 2014). Fault zones have more recently been the focus of significant interest, as shown in a number of recently published studies (*e.g.* Buatier *et al.*, 2012, 2015; Lacroix *et al.*, 2012; Trincal *et al.*, 2014; Schleicher *et al.*, 2015; Abd Elmola *et al.*, 2017) combining structural geology, petrology, clay mineralogy and geochemistry.

The aim of the present study is to determine the conditions for allochemical or isochemical formation of clay minerals in two thrust zones. Because it was not possible to distinguish the fault core from the damage zone without detailed fracture mapping in the study area, the term 'fault zone' was used to describe the structures investigated in this study. Both tectonic structures affect well-lithified sandstones and mudstones in a low-grade diagenetic setting. The thrusts studied are the Whakataki and Adams-Tinui faults located within the Hikurangi subduction wedge, onshore from the Wairarapa Coast, eastern North Island of New Zealand (Fig. 1). The onshore locations of the faults allow the study of the mineralogical and chemical compositions of samples in the fault zones and the determination of the maximum temperature conditions experienced. These results allow discrimination of the various origins of fault gouge clays by: (1) metasomatism from migrating fluids; (2) *in situ* diagenetic formation (precipitation); and (3) physical grinding during tectonic activity and subsequent diagenetic neoformation by deformation catalysis. X-ray diffraction also allows the determination of the swelling or non-swelling potential of clays as well as the clay mineral species and polytypism. This helps us to understand the various permeability and rheology conditions in faults at similar strain and stress geometries and strain rates. Moreover, grade of metamorphism may be evaluated by the determination of IC (*via* KI) and chlorite 'crystallinity' (*via* Árkaï index [AI]), as well as with the use of a chlorite geothermometer (*e.g.* Bourdelle *et al.*, 2013), because the chemical composition of chlorite is sensitive to pressure and temperature. These various methods will be combined on the same sample mineral and also combined with optical methods on organic matter reflectance to allow reconstruction of the pressure and temperature evolution of the fault zones. Due to varying reaction kinetics, different clay mineral indicators for determining metamorphism may display different steps of a pressure (P)–temperature (T)–time (t) path (Abad *et al.*, 2003b). For example, studies involving chlorite and illite 'crystallinities' have shown various evolution pathways as a function of the cation activity of essential cations such as K^+, Mg^{2+} and Fe^{2+} in pore fluids (Warr & Cox, 2016). A multi-method investigation of clay minerals and organic matter, combined with maturity modelling where possible, is recommended for determining the pressure- and temperature-dependent alteration histories of faults within tectonically active basins (Allen & Allen, 2005; Ferreiro Mählmann *et al.*, 2012). In this study, temperatures obtained with the chlorite geothermometer are compared to those obtained with organic-matter reflectance.

https://doi.org/10.1180/clm.2018.46 Published online by Cambridge University Press

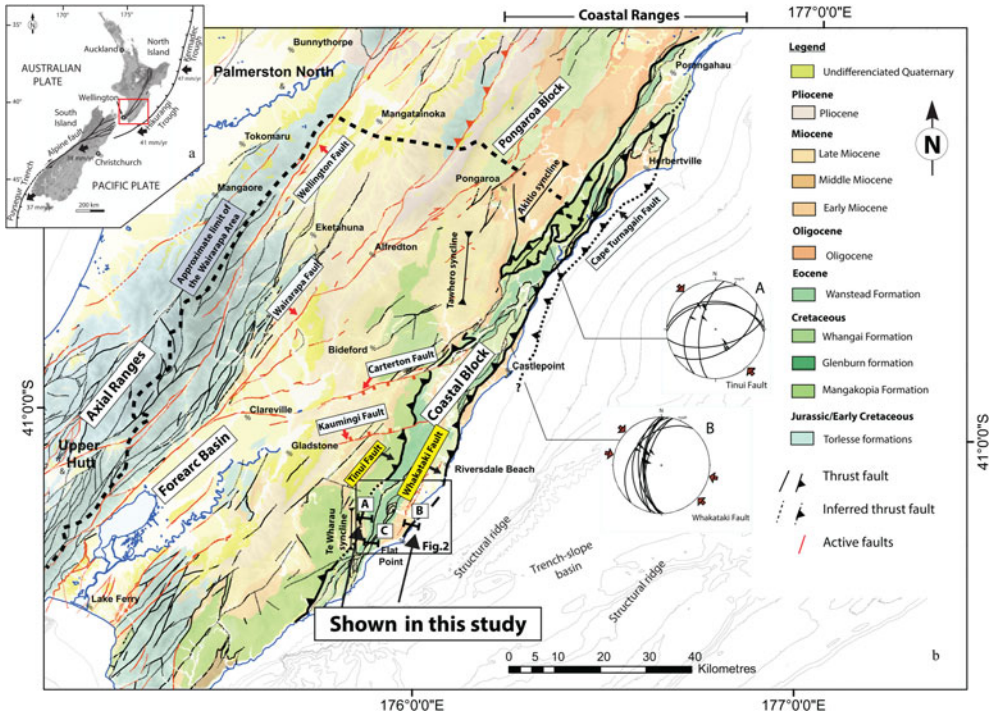

FIG. 1. (a) Plate tectonic setting of New Zealand showing the location of the study area. (b) Simplified structural map of the Wairarapa area (modified from Chanier *et al.*, 1999; Lee & Begg, 2002) and stress tensor analysis (Schmidt net, lower hemisphere) showing the main directions of principal horizontal shortening (red arrows) attributed to Plio-Quaternary deformation for the Adams-Tinui and Whakataki faults (from Bailleul *et al.*, 2013). The map shows the location of the two studied thrusts: the Whakataki and the Adams-Tinui faults. See cross-sections A, B and C in Fig. 3 and text for explanations.

GEOLOGICAL SETTING

General overview

The East Coast Basin (ECB) is located on the Hikurangi active margin, where the Pacific Plate is subducted below the Australian Plate (Fig. 1). The Hikurangi subduction wedge is composed of deformed Jurassic to Palaeogene sedimentary rocks, overlaid by the less deformed Neogene syn-subduction marine rocks of the ECB (Lewis & Pettinga, 1993). Onshore, in the Coastal Ranges of the eastern North Island of New Zealand, Neogene rocks form a succession of elongated synclines, separated by structural ridges, parallel to the subduction front (*e.g.* Lewis & Pettinga, 1993; Nicol *et al.*, 2007; Bailleul *et al.*, 2013).

Tectonic history

Since the onset of subduction (*ca*. 25 Ma ago), polyphase deformation has been responsible for the development of the Coastal Ranges with their complex stratigraphy disrupted by multiple structures. Three main phases of Neogene deformation have been reported:

(1) An Early Miocene to early Middle Miocene (*ca*. 17.5–15.0 Ma) compressional phase. This tectonic episode began in the southern part of the Coastal Ranges with the seaward emplacement of thrust-sheets (*ca*. 25–18 Ma) followed by E–W contraction responsible for extensive reverse faulting, folding and development of trench-slope basins bound by structural highs (Chanier & Ferrière, 1989, 1991; Rait *et al.*, 1991; Bailleul *et al.*, 2013).
(2) A Middle–Late Miocene period (*ca*. 15.0–6.5 Ma) of widespread subsidence (*e.g.* Chanier *et al.*, 1992, 1999; Bailleul *et al.*, 2013). This phase was coeval with normal faulting and syn-sedimentary gravitational collapse and

https://doi.org/10.1180/clm.2018.46 Published online by Cambridge University Press

was attributed to a 5–10-Myr period of tectonic erosion over the whole subduction margin (Chanier *et al.*, 1992, 1999). The extensional deformation appears to have occurred mainly upslope of the margin and contemporaneously with the downslope development of a frontal imbricated thrust wedge (Bailleul *et al.*, 2013).

(3) A tectonic inversion during a renewed compressional phase from 6.5 Ma to present day (*e.g.* Bailleul *et al.*, 2013). During this late Neogene to present-day contractional period (Chanier, 1991; Nicol *et al.*, 2002, 2007; Nicol & Beavan, 2003), margin deformation was dominated by regional folding and mainly landward-dipping reverse faulting (Fig. 1). This led to the uplift and emergence of the Coastal Ranges, including the Wairarapa Region where the study area is located (Nicol *et al.*, 2002, 2007; Bailleul *et al.*, 2013).

The Adams-Tinui and Whakataki faults

In the study area, the main structures are sub-parallel to the subduction front, typically oriented NNE–SSW. Miocene marine strata are generally exposed within elongated wide synclines bounded by highly deformed basement (lithified rocks older than Late Cretaceous) structural highs affected by reverse faults, mainly dipping to the WNW. One of the structural highs, the Coastal Block, shows two regional NNE–SSW fault zones: the Adams-Tinui fault and the Whakataki fault (*e.g.* Lee & Begg, 2002).

The Adams-Tinui fault was responsible for eastward thrusting of Early Cretaceous rocks over Late Cretaceous–Paleogene strata, and the Whakataki fault was responsible for seaward thrusting of Late Cretaceous and Eocene rocks over Early Miocene flysch deposits (Chanier, 1991). The Whakataki fault acts as the eastern boundary of the Coastal Block (Moore, 1988). The Whakataki fault and possibly the Adams-Tinui fault appear to have accommodated Quaternary displacement. Approximately 10 km north of Castlepoint, the Whakataki fault displaces Quaternary marine terrace deposits (Bailleul *et al.*, 2013). The most recent striations on the Adams-Tinui and Whakataki faults indicate mainly dip-slip motion and reveal a SE–NW trend of principal shortening direction (stereoplots A and B in Fig. 1). This shortening direction is similar to the main directions of post-Pliocene shortening over the whole area (Bailleul *et al.*, 2013). Earlier deformations along these fault zones are expressed in deformation patterns in fault crush zones that correspond to the soles of major nappes from the Coastal Ranges. They indicate a N–S to NW–SE direction of thrusting that is attributed to the earliest Miocene deformation in the Flat Point area (Chanier, 1991; Chanier & Ferrière, 1991), such as in the Akitio area (Delteil, 1996). These major faults from the inner subduction wedge have undergone a complex polyphase evolution with several steps of compression and seaward thrusting.

Stratigraphy

The Jurassic to Early Cretaceous Torlesse formation (C_1 in Fig. 2) is composed of metasedimentary rocks deposited in an accretionary prism setting during earlier subduction processes (George, 1990, 1992). It consists of a well-indurated rock suite of predominantly sandstones and mudstones with some interbedded layers of spilitic basalt, tuff, chert and very rare limestones (Suneson, 1993). The Late Cretaceous to early Palaeocene section is a stratiform succession of Glenburn ($C_2 + C_3$) and Whangai (C_4) Formations (Fig. 2). The Glenburn formation ($C_2 + C_3$) consists of dominantly alternating conglomerates, with sandstones and siltstones representing coarse-grained turbidite deposits. The total thickness of the Glenburn formation has been estimated locally to be >1000 m. The Whangai formation (C_4 in Fig. 2) is a massive micaceous siltstone/shale formation with occasional glauconite sandstone beds and magmatic dykes. The formation, which is up to ~1000 m thick, is mostly siliceous at its base (Campanian–Maestrichtian times) and becomes calcareous towards the top of the series, which is dated Palaeocene in age. The Palaeocene, and the Late Maestrichtian, show locally, some pelagic limestones alternating with beds of glauconite sandstones (Chanier *et al.*, 1990). In the most distal tectonic units, the Palaeocene is characterized by the development of organic-rich shales (Waipawa Black Shale), which are known to be the main source rock within the ECB (*e.g.* Field *et al.*, 1997; Lee & Begg, 2002; Hollis *et al.*, 2014). The Waipawa formation ranges from a few metres to ~50 m in thickness and is typically composed of non-calcareous to weakly calcareous dark chocolate-brown micaceous and sulfurous mudrocks with fine organic material scattered throughout. The Waipawa Black Shale is characterized by a high total organic

https://doi.org/10.1180/clm.2018.46 Published online by Cambridge University Press

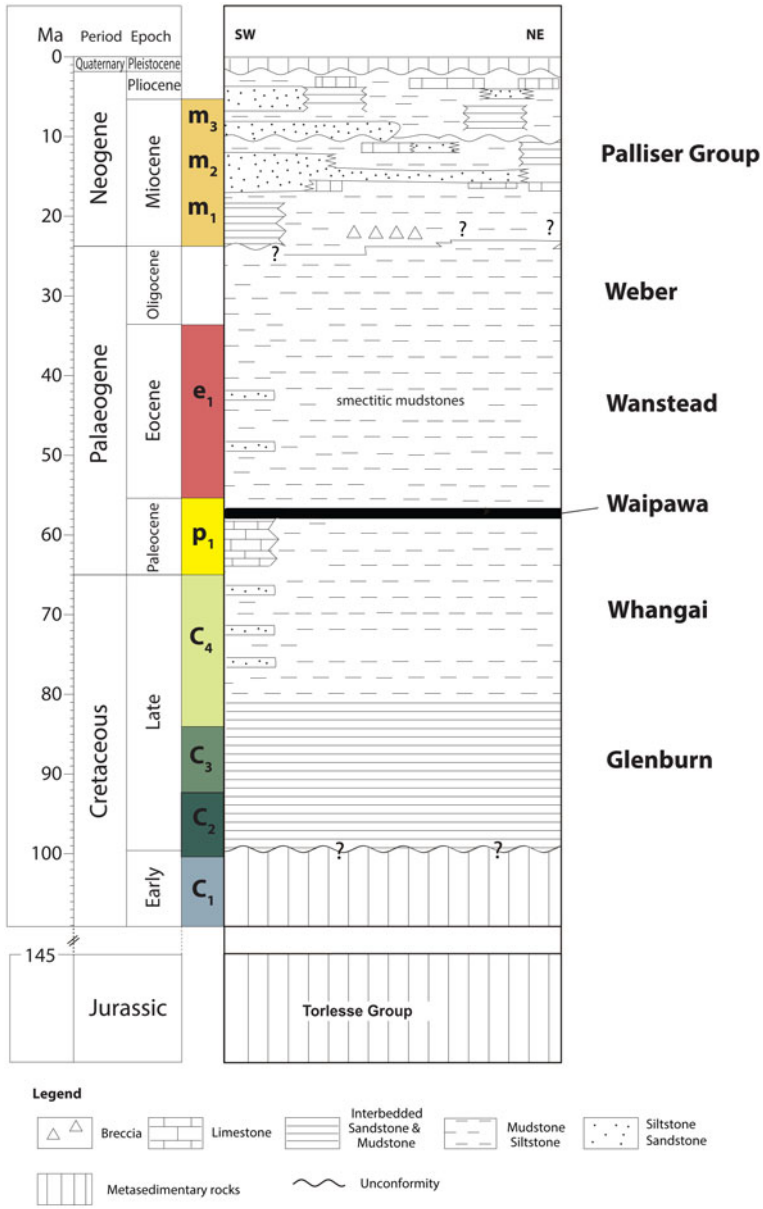

FIG. 2. Regional chronostratigraphic chart of the Wairarapa area (based on Field *et al.*, 1997).

carbon content and a high hydrogen index (Hollis *et al.*, 2014). During the Eocene–Oligocene period, the sedimentation was dominantly hemipelagic to pelagic, with notable deposition of marls and pelagic limestones. The Eocene Wanstead Formation comprises mainly smectite-rich calcareous mudstones with locally interbedded glauconite sandstones (*e.g.* Chanier & Ferrière, 1991; Field *et al.*, 1997; Lee & Begg, 2002).

Sampling sites

The sampling sites where the Adams-Tinui and the Whakataki faults crop out are located to the south of

https://doi.org/10.1180/clm.2018.46 Published online by Cambridge University Press

the Te Wharau area and to the north of the Flat Point area, respectively (Fig. 3).

The Whakataki fault in the Flat Point area

In the Flat Point area (Fig. 3), undifferentiated Late Cretaceous to Palaeocene formations, dipping to the northwest, have been thrusted over the Early Miocene (Waitakian–Otaian NZ stage) turbiditic formation of the Flat Point Flysch (Chanier & Ferrière, 1991), which is equivalent in age and facies to the Whakataki formation further north. This thrust zone has been named locally as the Flat Point fault (Chanier & Ferrière, 1989; Chanier, 1991) and is considered to be the southern prolongation of the Whakataki fault, which is one of the major thrust faults of the Wairarapa Coastal Ranges (Chanier & Ferrière, 1991). This thrust fault is N025°E directed and is presently dipping about 75° towards the northeast. It corresponds to one of the main thrusts associated with the onset of subduction in the earliest Miocene (Chanier & Ferrière, 1991; Rait *et al.*, 1991) which were later steepened on the limb of regional folds developed during Pliocene to Quaternary times (Chanier, 1991). This fault zone has therefore been regarded as a thick palaeo-decollement zone that participated in the tectonic stacking of kilometre-thick margin units. The decollement is composed of Eocene smectite clays with a scaly fabric containing blocks of glauconite sandstones that were originally interbedded with the clays of the Wanstead formation (Figs 3, 4).

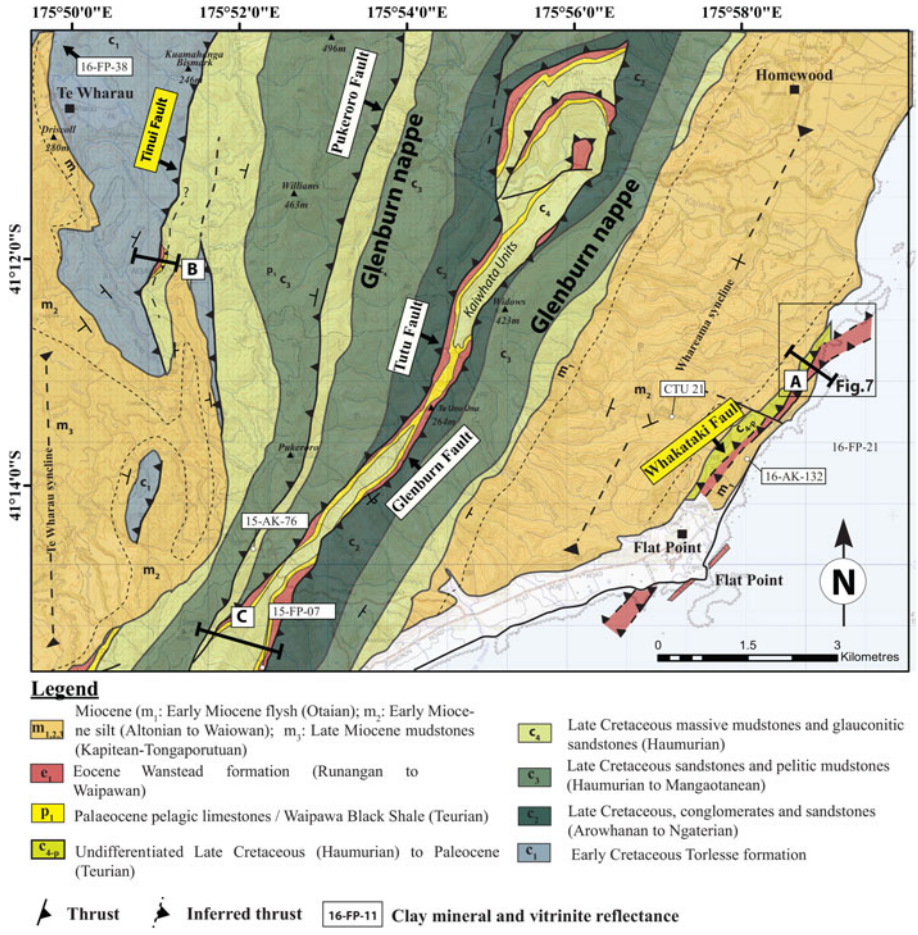

FIG. 3. Onshore geological map (from Chanier, 1991).

https://doi.org/10.1180/clm.2018.46 Published online by Cambridge University Press

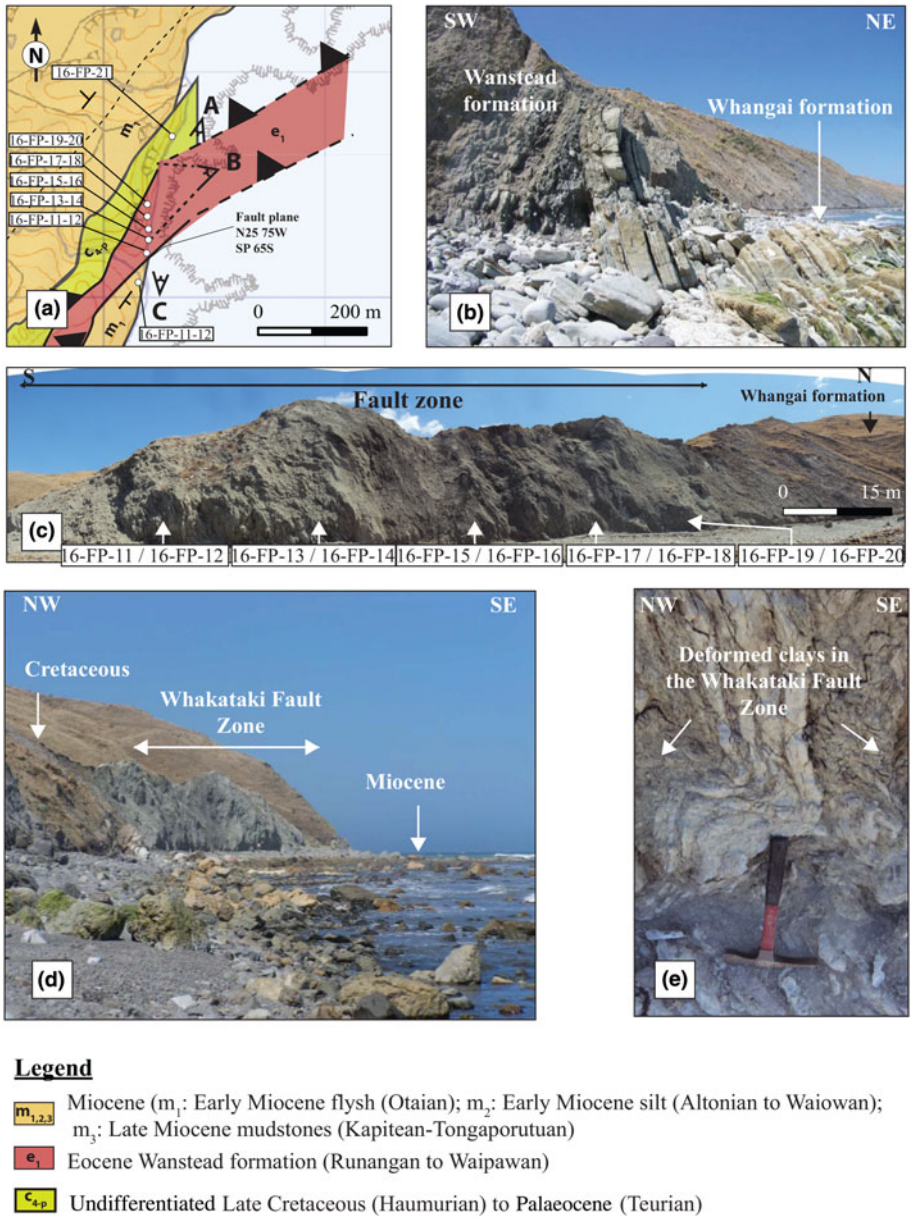

FIG. 4. (a) Detailed geological map of the Whakataki fault in the Flat Point area and location of the studied samples. (b) Field photograph of a faulted contact between the Eocene Wanstead Formation and the Late Cretaceous Whangai formation. (c) Panoramic view of the Eocene Wanstead formation in the Whakataki fault and location of samples 16-FP-11 to 16-FP-20. (d) Panoramic view of the fault zone, where the Cretaceous formation is thrusted over the Early Miocene formations. (e) Zoomed-in view of the folding and deformation in the Eocene Wanstead formations in the Whakataki fault zone.

The Adams-Tinui fault in the Te Wharau area

In the Te Wharau area, the Adams-Tinui fault crops out 3 km to the southeast of the Te Wharau settlement. The Early Cretaceous Torlesse Formation thrusts eastward on Late Cretaceous to Palaeocene rocks (Figs 3, 5a,b). The Early Cretaceous Torlesse formation is composed of metasedimentary rocks,

https://doi.org/10.1180/clm.2018.46 Published online by Cambridge University Press

predominantly greywackes and red mudrocks. The underlying Late Cretaceous Whangai units on the footwall are composed of massive deformed mudstones and sandstones. The deformation zone is composed of the Eocene smectite clays and glauconite sandstones of the Wanstead Formation, which has also been described for the Whakataki fault. A slaty cleavage (Fig. 5c) is visible in the outcrop with the presence of layers rich in phyllosilicates and an elongated fabric of phyllosilicate grains in the finer-grained components.

To the east of the fault zone, the Palaeocene corresponds to the organic-rich Waipawa Formation. The core zone of the Adams-Tinui fault comprises deformed mudstones with slaty cleavage and is 2 m wide. The fault zone in the footwall is 50 m wide and is formed by a clayey matrix containing slightly deformed sandstones and mudstones (Fig. 5a,c).

MATERIALS AND METHODS

In the Whakataki fault, ten samples were collected in the footwall, hanging wall (fault zone) and core zone (fault gouge) of the fault (Fig. 4a). This enabled the characterization of clay minerals from representative mudstones and sandstones all along the fault zone, reflecting various degrees of deformation. In the fault zone, the sampling was undertaken every 15 m. We also added two samples from the thrusted Early Miocene (Otaian) Whakataki formation and from the Eocene Wanstead formation for vitrinite and solid bitumen reflectance studies.

In the Adams-Tinui fault, ten samples were collected in the footwall, hanging wall (fault zone) and core zone of the fault, enabling the same characterization of clay minerals as at the Whakataki fault. We sampled in the fault zone (more than 10 m away from the core zone) every 15 m. We also included three samples from the organic-rich Waipawa formation, one from the Late Cretaceous Whangai formation and one from the Eocene Wanstead formation for vitrinite and solid bitumen reflectance studies.

X-ray diffraction

In pelitic rocks and coarser siliciclastic rocks (except greywacke), diagnostic minerals and mineral assemblages of the very-low-grade metamorphic facies zone

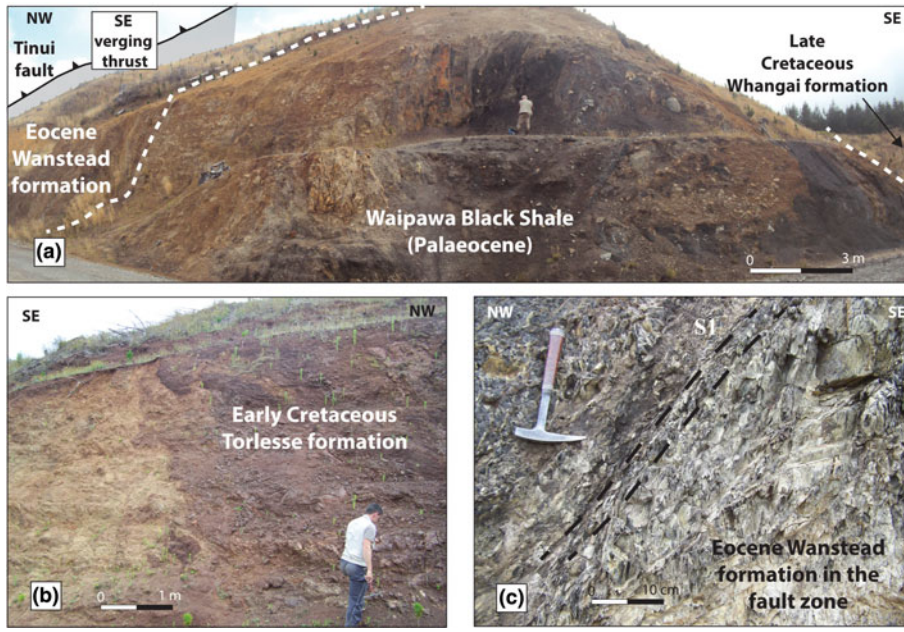

Fig. 5. (a) Panoramic view of the Adams-Tinui fault zone. (b) Early Cretaceous Torlesse Formation outcropping in the Adams-Tinui fault zone. (c) Field photograph of the deformed Eocene Wanstead Formation in the damage zone of the Adams-Tinui fault. See the pervasive, parallel layering of the finer-grained minerals (slaty cleavage) in a NE–SW direction.

https://doi.org/10.1180/clm.2018.46 Published online by Cambridge University Press

are scarce and only found in rocks with a very specific geochemical composition (Frey, 1987). In these rocks, the transitions from non-metamorphic to low-grade (referring to the term 'greenschist facies' of Winkler, 1979) and from the very-low-grade ('chlorite zone' of Tilley, 1925) to low-grade metamorphic zone ('biotite zone' of Barrow, 1893) take place through the diagenetic zone, the anchizone and the epizone (*cf.*, Kisch, 1987), with each zone being characterized by specific KI values (Kisch, 1987; Árkai *et al.*, 2003, 2007). The upper limit of the anchizone is defined in many metapelites by the occurrence of chloritoid, an index mineral of the greenschist facies (Kübler *et al.*, 1979). The anchizone is most correlated with the sub-greenschist and sub-blueschist facies *vs.* anthracite coal rank, as shown by Ferreiro Mählmann & Le Bayon (2016; see also Kisch, 1987). In the present study, the 10 Å FWHM values refer to the IC of raw data, whereas KI corresponds to the values after calibration against Kübler's scale (Kübler, 1967). We refer to the chlorite 'crystallinity' data in the same way, using the raw data for the 7-Å FWHM and the AI (Árkai, 1991) as measured after calibration.

Illite and chlorite 'crystallinities' are considered to be functions of crystallite thickness, the number of lattice defects (Merriman *et al.*, 1990) and the peak interference, if any, with discrete smectite or illite-smectite mixed-layer compositions (Ferreiro Mählmann *et al.*, 2012). Temperature is thought to be the main factor controlling IC, but other parameters such as lithology, time, tectonic stress and fluid:rock ratio probably have important effects (see Frey, 1987; Árkai *et al.*, 2002, Mullis *et al.*, 2017). A recent study from Warr & Cox (2016) has confirmed that clay 'crystallinity' (for illite and chlorite) provides a useful method for characterizing regional grades of low-temperature metamorphism (Árkai *et al.*, 1995): illite and chlorite 'crystallinities' can be related with a nonlinear regression curve. This nonlinearity is presumed to be due to the presence of diagenetic 001 illite reflections in illite-smectite phases. For higher grades, the relation between illite and chlorite 'crystallinities' is more linear (Potel *et al.*, 2006).

Table 1. Metapelitic zone boundaries (after Merriman & Frey, 1999) for KI and AI values after Warr & Ferreiro Mählmann (2015).

Metapelitic zone	KI	AI
Diagenesis	0.42	0.35
Lower anchizone	0.30	
Upper anchizone	0.25	0.30
Epizone		

Experimental conditions. X-ray diffraction analysis was performed using a D8-Advance Bruker-AXS (Siemens) diffractometer, Ni-filtered Cu-$K\alpha$ radiation at 40 kV and 40 mA, a primary soller slit of 2.5°, a divergence slit of 0.6 mm and a secondary soller slit of 2.5°, with a detector slit of 0.1 mm and an antiscattering slit of 0.6 mm. Samples were crushed with an agate pestle and mortar. Clay mineral separation was conducted using the techniques described by Potel *et al.* (2016). To minimize the effect of possible detrital clay minerals, we avoided long grinding processes (<30 s) and repeated the settling procedure for the ≤2 μm fraction twice. Quantitative phase analysis based on reference intensity ratio values were performed on randomly oriented whole-rock powders with a step length of 0.5° and a scan speed of 0.014°/s over the range 3–70°2θ for whole-rock compositions. The uncertainty is estimated to be ~5%.

Illite and chlorite indices. Ten samples were collected in the Whakataki fault zone and ten samples were collected in the Adams-Tinui fault zone (Figs 4, 5). Clay mineral separation was conducted using the techniques described by Schmidt *et al.* (1997), following the recommendations of Kisch (1991), and according to the standard techniques suggested by Ferreiro Mählmann & Frey (2012). For the XRD analyses of the ≤2.0 μm fractions, oriented specimens were prepared and then examined in an air-dried state after solvation with ethylene glycol and after heating (550°C). For air-dried, ethylene glycol-solvated and heated samples, measurements were performed with a scanning step of 0.5° and a speed of 0.01°/s per step over the range 3–35°2θ. The IC was calculated using the software *DIFFRACPlus EVAL* v. 12.0 (by Bruker AXS). The IC values were standardized using the crystallinity index-standard (CIS) samples of Warr & Rice (1994) ($KI_{CIS} = 2.5734 \times IC_{ULS} - 0.1348$). The IC_{ULS} is the FWHM value measured at UniLaSalle Beauvais (ULS). The KI is used to define the limits of metamorphic zones, following the recommendations for KI calibration of Ferreiro Mählmann & Frey (2012) and the CIS–KI transformation formalism of Warr & Ferreiro Mählmann (2015). The zone boundary values were chosen as follows: $KI = 0.25\Delta°2\theta$ for the epizone to high anchizone boundary, $KI = 0.30\Delta°2\theta$ for the high to low anchizone boundary and $KI = 0.42\Delta°2\theta$

https://doi.org/10.1180/clm.2018.46 Published online by Cambridge University Press

for the low anchizone to diagenetic zone boundary (Table 1). The same experimental conditions were used to determine chlorite 'crystallinity' on the (002) peak, where (ChC(002)) corresponds to the FWHM intensity values of the second (7-Å) basal reflection of chlorite. The ChC(002) measurements were also standardized with the CIS sample set of Warr & Rice (1994) and expressed as the AI according to the formalism proposed by Guggenheim *et al.* (2002): AI = 1.621 × ChC(002) + 0.006. The anchizone boundaries for the AI were defined by correlation with the KI at 0.30Δ°2θ for the epizone to anchizone boundary and 0.35Δ°2θ for the anchizone to diagenetic zone boundary. The smallest FWHM possible to measure is 0.08Δ°2θ.

The kaolinite 'crystallinity' was measured as the FWHM on the 001 kaolinite peak in the absence of chlorite, following the recommendation of Aparicio and Galán (1999).

Scanning electron microscopy with energy-dispersive X-ray spectroscopy. Chemical compositions of chlorites were analysed and used for chlorite geothermometric determinations. The compositions were determined with an energy-dispersive X-ray (EDX) scanning electron microscope (SEM) (Hitachi S3400N SEM equipped with a Thermo Ultradry EDX probe at ULS). A ZAF-type correction procedure was used for all data reduction and all Fe was assumed to be ferrous. Carbon-coated, polished, thin sections were analysed using a 60-nA beam current, an accelerating voltage of 15 kV, an acquisition time of 30 s and an EDX activation volume of 5 μm^3 relative to an average clay size of 10 μm in width.

Chlorite geothermometer. The chlorite geothermometry was carried out using the geothermometer of Bourdelle *et al.* (2013). This geothermometer is applicable to all low-temperature chlorite compositions (T <350°C; P <4 kbar), but specifically for Si-rich compositions that characterize the diagenetic chlorites encountered in the studied area. To ensure the appropriate composition of chlorites, the chlorite chemistry was determined with the EDX-SEM device using polished, thin sections. From these results, the cationic repartition in the structure is defined, assuming an ordered distribution on the crystal sites, thus determining the ideal activities of end-members. The semi-empirical $T = f(\log K)$ geothermometer is formulated as a function of K, the equilibrium constant of the end-member-component reaction describing the chlorite + quartz equilibrium (function as activity) according to Bourdelle *et al.* (2013; see equation 1):

$$T(^{\circ}\mathrm{C}) = \frac{9400}{23.40 - \log x} - 273 \qquad (1)$$

$$\text{where} \quad x = \frac{(a^3_{Mg\text{-}Am})}{(a_{Mg\text{-}ChlS})(a^3_{Mg\text{-}Sud})}$$

and *Mg-Am* = Mg-amesite, *Mg-ChlS* = Mg-chlorite semi-ordered and *Mg-Sud* = Mg-sudoite.

Vitrinite reflectance

The chemical kinetics that governs maturation is still thought to be strongly temperature dependent (*e.g.* Taylor *et al.*, 1998; Polissar *et al.*, 2011). In addition to vitrinite reflectance (VR) (Le Bayon *et al.*, 2011), other optical properties of organic matter are pressure dependent (as for vitrinite; see *e.g.* Chandra, 1965; Dalla Torre *et al.*, 1997). The recognition of characteristic optical changes has been used recently to predict various pressure conditions (Ferreiro Mählmann & Le Bayon, 2016). The VR determinations were made on a Leitz microscope (Ortholux 2 POL BK) with a 125× oil-immersion objective (10× oculars) using monochromatic polarized light (546 nm) and a Leitz MPV photomultiplier at the Technische Universität Darmstadt. In all cases, the minimum reflectance (R_{min}%) and maximum reflectance (R_{max}%) of vitrinite were determined if bireflectance was observed. In most cases, bireflectance was not developed and thus random reflectance (R_r%) was used. Different temperature–pressure–thermal gradient conditions can be recognized using the first appearance of bireflectance with increasing maturity (Ferreiro Mählmann & Le Bayon, 2016). The photomultiplier is used to measure the reflectance intensity, which is determined through comparison with standards of known reflectance (yttrium aluminium garnet single crystal for the range of VR = 0.2–2.0%; gallium gadolinium garnet single crystal for the range of VR = 1.0–3.0%).

RESULTS

The mineralogy of the samples studied is given in Table 2. Mineral abbreviations follow Kretz (1983). The Whakataki samples consist of quartz (Qtz) and feldspar (Fsp) and/or calcite (Cal) and clay minerals. In the <2 μm size fractions, illite-muscovite predominates in association with montmorillonite (Mt) and/or kaolinite (Kln) and/or vermiculite (V). The Adams-Tinui samples consist of quartz (Qtz) with clay

https://doi.org/10.1180/clm.2018.46 Published online by Cambridge University Press

TABLE 2. Clay mineralogy and clay mineral index data of studied samples from the Whakataki and Adams-Tinui faults (expressed in percentages) and the FWHM of the (001) illite/muscovite reflection and (002) chlorite reflection and their values after calibration in KI and AI, respectively. For the locations of the samples, see Fig. 3.

							Mineralogy							I-Ms		Chl-Kln	
	Sample	Age	Nomenclature	Qtz	Fsp	Cal	Gp	Cbz	Mt	V	Kln	I-Ms	Chl	FWHM (001)	KI	FWHM (002)	AI
Whakataki fault	16-FP-12	Eo	Sandstone	19	12	69	–	–	–	–	–	–	–	–	–	–	–
	16-FP-13	Eo	Mudstone	20	37	15	–	–	1	1	7	19	–	0.24	0.54	0.40	–
	16-FP-14	Eo	Sandstone	19	33	29	–	–	1	1	3	14	–	0.22	0.48	0.32	–
	16-FP-15	Eo	Mudstone	21	44	20	–	–	1	2	4	8	–	0.23	0.52	0.28	–
	16-FP-16	Eo	Mudstone	21	36	3	–	–	3	1	15	20	–	–	–	0.32	–
	16-FP-17	Eo	Mudstone	20	41	4	–	–	2	1	12	20	–	0.22	0.49	0.29	–
	16-FP-18	Eo	Mudstone	35	37	6	–	–	1	1	8	12	–	0.30	0.68	0.26	–
	16-FP-19	Eo	Sandstone	46	10	44	–	–	–	–	–	–	–	–	–	–	–
	16-FP-20	Eo	Mudstone	20	50	–	–	–	1	3	9	18	–	0.25	0.55	0.27	–
	16-FP-21	EMio	Mudstone	23	30	–	–	–	1	–	–	46	–	0.18	0.39	–	–
Adams-Tinui fault	16-FP-22	Eo	Mudstone	40	–	58	–	–	–	–	1	1	–	0.19	0.40	0.39	–
	16-FP-23	Eo	Mudstone	22	19	5	8	–	1	1	2	40	2	0.30	0.62	0.24	–
	16-FP-24	LCr	Mudstone	19	26	3	–	–	3	2	12	36	–	0.21	0.44	0.43	–
	16-FP-25	LCr	Mudstone	26	28	–	4	–	1	1	10	29	–	0.20	0.43	0.46	–
	16-FP-32	Eo	Mudstone	17	50	–	–	–	3	2	12	16	–	0.22	0.48	0.51	–
	16-FP-33	LCr	Mudstone	13	56	1	–	–	1	1	10	18	–	0.20	0.44	0.49	–
	16-FP-35	ECr	Black shales	1	85	–	–	6	–	3	5	–	–	–	–	–	–
	16-FP-36	ECr	Black shales	23	32	–	–	–	–	–	10	23	11	0.45	0.92	0.27	0.44
	16-FP-37	ECr	Black shales	19	28	–	–	–	–	1	–	43	9	0.44	0.90	0.27	0.45
	16-FP-38	ECr	Black shales	16	56	–	–	–	–	–	–	11	17	0.31	0.63	0.27	0.45

Key to the abbreviations (from Kretz, 1983): Qtz = quartz; Fsp = feldspar; Cal = calcite; Gp = gypsum; Cbz = chabazite; Mt = montmorillonite; V = vermiculite; Kln = kaolinite; I = illite; Ms = muscovite; Chl = chlorite; Eo = Eocene; EMio = Early Miocene; LCr = Late Cretaceous (Whangai); ECr = Early Cretaceous (Torlesse).

minerals and/or feldspar (Fsp) with calcite (Cal) and gypsum (Gp) and sporadic chabazite, especially in sample 16-FP-35 from near the western fault plane. In the <2 μm grain fraction, illite-muscovite predominates in association with kaolinite (Kln) and/or montmorillonite (Mt) and/or vermiculite (V) and/or chlorite (Chl) (Fig. 6). Chlorite is present in the Eocene and Torlesse rocks (Early Cretaceous).

AI values were only determined for samples 16-FP-36, 16-FP-37 and 16-FP-38, where the chlorite content and peak allowed the calculation of this parameter. AI values in the Adams-Tinui fault had an average of 0.45Δ°2θ, corresponding to diagenesis.

Kaolinite 'crystallinity' was determined from the air-dried diffractogram (Table 2, Fig. 7), with values ranging from 0.26 and 0.51Δ°2θ.

FWHM characteristics of the phyllosilicates

The KI and AI were calculated from the FWHM of illite-muscovite and chlorite peaks on the air-dried XRD traces, respectively. The KI and AI values are listed in Table 2 and the spatial distributions of samples are shown in Fig. 3.

In the Whakataki fault, KI values range from 0.68Δ° 2θ to 0.39Δ°2θ, corresponding to diagenesis to lower anchizone. In the Adams-Tinui fault, the KI shows a broader range of values between 0.92Δ°2θ and 0.40Δ° 2θ, indicative of diagenesis to lower anchizone. Due to the broadening of the peak and the overlapping with other phases, the KI was not calculated for samples 16-FP-11 and 16-FP-16. The KI values are higher in older formations (Early Cretaceous) than in younger formations (Early Miocene, Eocene and Late Cretaceous).

Phyllosilicate chemistry

Due to the small grain size of the phyllosilicates (<10 μm), special care was taken to differentiate between detrital and newly formed metamorphic grains to avoid minerals of uncertain origin. Neoformed K-white mica may be observed as fine-grained laths (<1 μm wide) (Fig. 6a), whereas detrital K-white micas (not measured) are observed as coarser and kinked grains (between 5 and 10 μm wide) (Fig. 6b). Chlorite grains are present as aggregates of fibrous chlorite, with no evidence of detrital flakes (Fig. 6c).

Representative compositions of K-white mica are listed in Table 3. In a Si–Al_{tot} diagram (Fig. 8a), the analyses show a significant deviation from the Tschermak exchange line, with a large Si content. In

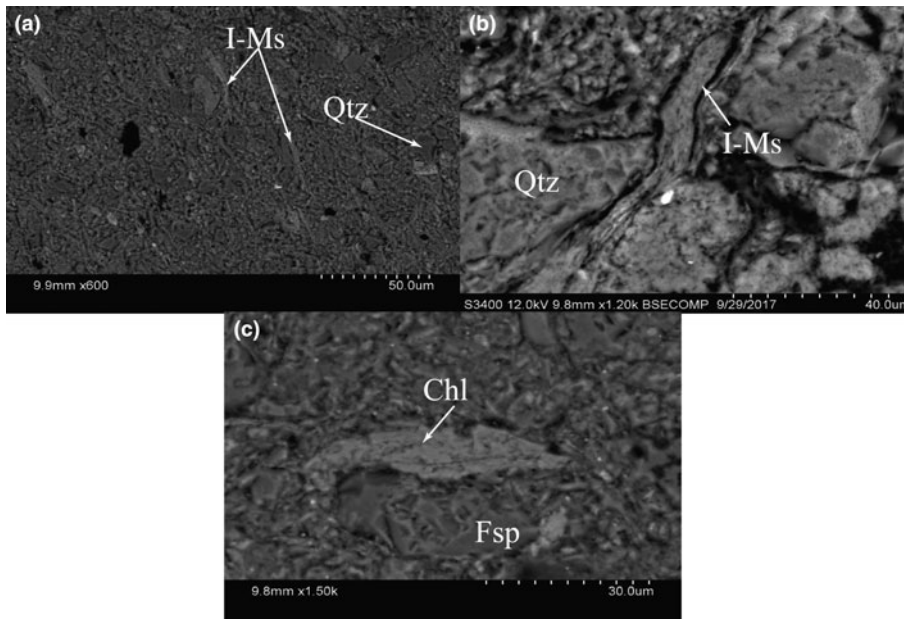

FIG. 6. SEM images of the phyllosilicates: (a) neoformed K-white micas (sample 16-FP-13); (b) detrital K-white micas (sample 16-FP-18); (c) chlorite (sample 16-FP-37).

https://doi.org/10.1180/clm.2018.46 Published online by Cambridge University Press

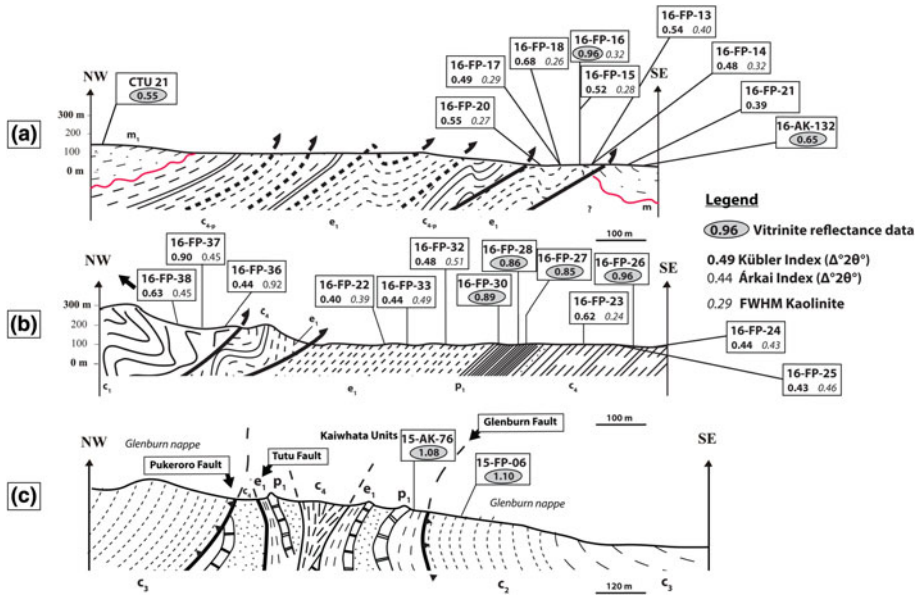

FIG. 7. Locations of the samples used in this study and the cross-sections. (a) Cross-section of the Whakataki fault in the Flat Point area. (b) Cross-section of the Adams-Tinui fault in the Te Wharau area. (c) Cross-section through the Kaiwhata units (Chanier & Ferrière, 1989) showing the structural complexity of this area.

addition to the Tschermak substitution (substitution of Si by Al), other substitutions or contaminations can be assumed. In Fig. 8b, on the basis of model calculations assuming various mixtures, a contamination of the analyses of mica by quartz can be assumed in certain samples, probably due to the small grain size (<10 μm) and the instability of the mica under the electron beam.

In Fig. 8c, the K-white mica analyses fall in a cluster between the muscovite–phengite and the muscovite–illite lines, indicating a small deficit in total interlayer cations (values range between 0.60 and 0.98 per formula unit [p.f.u.]; Table 3).

Minor chlorite was detected and analysed in samples 16FP17, 16FP32 and 16FP33, although it was not identified in XRD analyses, probably due to the detection limit of the technique. Compositions of chlorite (Table 4) fulfil the criterion of non-contamination ($\sum Ca + Na + K < 0.2$; Dalla Torre *et al.*, 1996). Using the classification of Zane & Weiss (1998), chlorites in the studied samples are mostly trioctahedral type I, where $X_{Mg} + X_{Fe} \geq X_{Al} + X_{vacancy}$. The Al^{VI}–Fe–(Mg + Mn) diagram revealed intermediate compositions between chamosite clinochlore and sudoite (Fig. 9a). X_{Mg} varies between 0.25 and 0.70.

The low total interlayer charge of the chlorite (<0.2 p.f.u.) indicates that smectite or illite impurities are negligible. The increase of (Al^{VI} – Al^{IV}) might be attributed to increasing sudoitic substitution (di-trioctahedral) (Árkai *et al.*, 2003), as is also indicated by the trend of the chlorite composition in Fig. 8a towards a sudoitic composition. Correlations observed for apparent octahedral vacancies with (Al^{VI} – Al^{IV}) (Fig. 9b) and apparent octahedral vacancies with the sum of octahedral divalent cations (Fig. 9c) prove the presence of sudoitic substitution in the analysed chlorites. In Fig. 9b,c, two groups of chlorites can be distinguished as a function of sample age (Cretaceous and Eocene). Fig. 9d demonstrates that, in addition to the Tschermak substitution, the di-trioctahedral substitution plays an important role in chlorites.

Vitrinite reflectance

The VR data from the Whakataki and Adams-Tinui faults are listed in Table 5. The VR obtained in the Whakataki fault (in Eocene sample 16-FP-16) shows a mean value of 0.96 R_r%. However, both samples (CTU21 in the Whareama syncline and 16-AK-132) coming from Miocene formations show smaller values (VR = 0.55 R_r% for CTU21 and VR = 0.65 R_r% for 16-AK-132). The VR obtained in the Adams-Tinui fault shows a value of 0.96 R_r% for the Late Cretaceous (Whangai) and a mean value of 0.87 R_r% for the Palaeocene formation. However, in the Glenburn

https://doi.org/10.1180/clm.2018.46 Published online by Cambridge University Press

TABLE 3. Representative chemical analyses of K-white micas based on 11 oxygen atoms.

Sample no.	16-FP-13		16-FP-17		16-FP-18		16-FP-21		16-FP-32		16-FP-33		16-FP-37	
n	27	SD	20	SD	7	SD	3	SD	8	SD	20	SD	10	SD
SiO_2	50.58	1.66	49.91	1.38	52.23	1.68	52.79	1.21	48.40	1.69	49.71	1.79	47.96	1.99
TiO_2	–	–	–	–	–	–	–	–	–	–	–	–	–	–
Al_2O_3	26.34	1.34	26.10	1.85	27.15	1.66	22.85	1.28	27.42	2.20	25.77	2.04	27.23	3.30
FeO	2.55	1.98	2.72	2.15	–	–	3.62	0.85	5.21	2.43	3.07	2.48	4.00	2.00
MnO	–	–	–	–	–	–	–	–	–	–	–	–	–	–
MgO	2.00	0.32	2.08	0.34	2.25	0.27	3.00	0.33	1.87	0.38	1.81	0.29	1.75	0.58
CaO	–	–	–	–	–	–	0.45	0.77	–	–	–	–	–	–
Na_2O	–	–	0.08	0.25	0.10	0.25	0.06	0.11	0.03	0.09	0.30	0.43	0.43	0.56
K_2O	8.35	0.72	8.98	0.76	7.79	0.93	6.24	0.84	7.08	0.48	9.11	0.87	8.62	1.29
Total	89.82	0.37	89.87	0.29	89.51	0.53	89.01	0.97	90.00	0.01	89.75	0.44	90.00	0.01
Structural formulae														
Si	3.52	0.08	3.49	0.07	3.57	0.10	3.67	0.04	3.39	0.09	3.50	0.10	3.38	0.14
Ti	–	–	–	–	–	–	–	–	–	–	–	–	–	–
Al^{IV}	0.48	0.08	0.51	0.07	0.43	0.10	0.33	0.04	0.61	0.09	0.50	0.10	0.62	0.14
Al^{VI}	1.68	0.08	1.65	0.10	1.76	0.05	1.54	0.09	1.66	0.12	1.63	0.10	1.64	0.13
Fe^{2+}	0.15	0.12	0.16	0.13	–	–	0.20	0.04	0.31	0.15	0.18	0.15	0.23	0.12
Mn	–	–	–	–	–	–	–	–	–	–	–	–	–	–
Mg	0.21	0.03	0.22	0.04	0.23	0.03	0.31	0.04	0.19	0.04	0.19	0.03	0.18	0.06
Ca	–	–	–	–	–	–	0.03	0.06	–	–	–	–	–	–
Na	–	–	0.01	0.03	0.01	0.03	0.01	0.01	–	0.01	0.04	0.06	0.06	0.08
K	0.74	0.07	0.80	0.07	0.68	0.09	0.55	0.08	0.63	0.04	0.82	0.08	0.78	0.12
t.i.c.	0.74	0.07	0.81	0.08	0.69	0.12	0.59	0.04	0.64	0.04	0.86	0.11	0.83	0.11
b_0		9.04		9.04		9.03		9.05		9.04		9.04		9.03
KI	0.54		0.49		0.68		0.39		0.48		0.44		0.90	

Calculations are based on 11 oxygen atoms (anhydrous basis).
b_0 values calculated after Guidotti *et al.* (1989).
t.i.c. = total interlayer cations (Ca + Na + K).

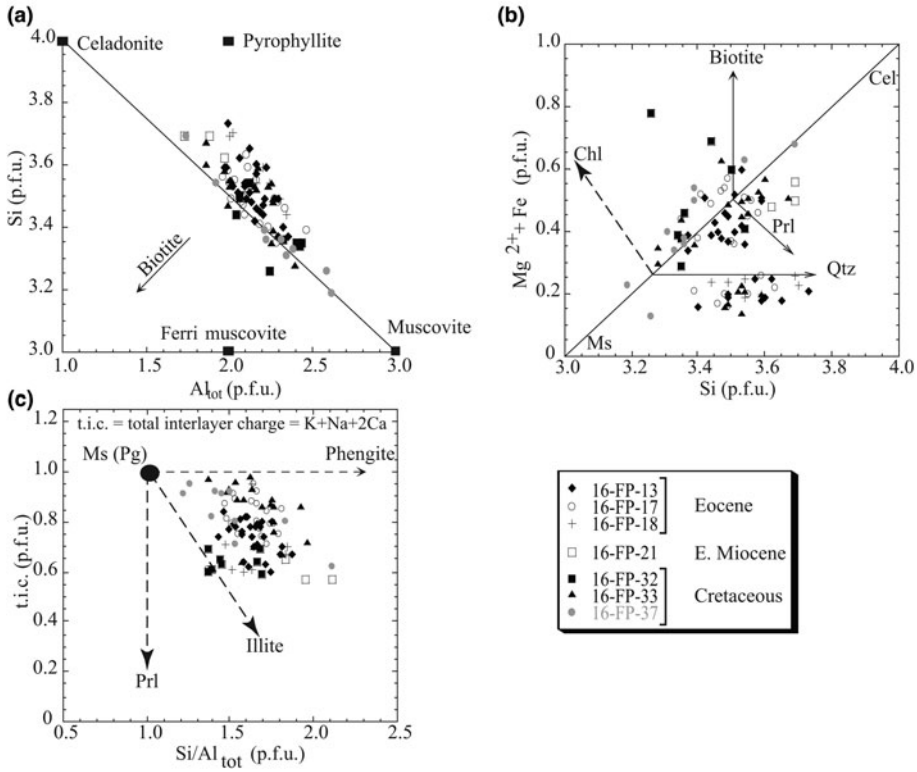

FIG. 8. (a–c) Compositional relationships of metamorphic dioctahedral white micas. Cation numbers and ratios were calculated from EDX analyses.

nappe (VR = 1.08 R_r% for 15-AK-76 and VR = 1.1 R_r% for 15-FP-06) and in the Kaiwhata unit (VR = 1.3 R_r% for 15-FP-07), the values are higher than in the fault zone. All of the samples analysed in this study do not show bireflectance due to low maturity.

DISCUSSION

For both the Whakataki and the Adams-Tinui fault zones, there is no relationship between stratigraphic age and KI value (Table 2, Fig. 10a). However, the highest diagenetic grade interpreted by KI value (AI values are only sporadically present) are observed in the older formation (Early Cretaceous) affected by the Adams-Tinui fault (Table 2). The KI values are not related directly to the sample location in the fault zone (Fig. 4). In contrast, a trend may be observed in the kaolinite 'crystallinity' values in the Adams-Tinui and Whakataki faults (Fig. 7). In the Whakataki fault, the values increase towards the fault, varying from 0.27 to 0.40Δ°2θ close to the fault. Previous work has shown that the increase in deformation close to the fault, where tectonic strain proceeds faster than recrystallization, favours a reduction in phyllosilicate crystal size (Giorgetti *et al.*, 2000; Abad *et al.*, 2003a). Hence, the kaolinite 'crystallinity' values follow this trend. In this study, most of the KI values are typical of the diagenetic zone, except for the KI values from the Early Miocene sample of the Whakataki fault zone (16-FP-21) and the Eocene sample (16-FP-22) of the Adams-Tinui fault sharing anchizone values. The presence of chabazite in sample 16-FP-35, the existence of kaolinite (Kln), montmorillonite (Mt), vermiculite (V) and illite-smectite (I-Sm) and the occurrence of microscopic glauconite in many samples confirm the low diagenetic grade, although the KI was not measured in the samples from the Whakataki fault zone. Chabazite crystallizes at 50–100°C (Deer *et al.*, 2013), which corresponds to the temperature range of diagenesis (0–230 ± 30°C; Ferreiro Mählmann & Le Bayon, 2016; Mullis *et al.*, 2017).

Although the KI is a useful index for showing gradual changes in grade of metamorphism, it should not be used as a precise geothermometer, as it provides

https://doi.org/10.1180/clm.2018.46 Published online by Cambridge University Press

TABLE 4. Representative structural formulae of chlorite based on 14 oxygen atoms.

Sample no.	16-FP-17		16-FP-18		16-FP-32 (1)		16-FP-32 (2)		16-FP-33		16-FP-37	
n	4	SD	5	SD	2	SD	2	SD	1	SD	18	SD
Si	3.24	0.02	3.28	0.15	3.29	0.09	3.16	0.06	3.15		3.16	0.14
Ti	–	–	–	–	–	–	–	–	–		0.01	0.04
Al^{IV}	0.76	0.02	0.72	0.15	0.71	0.09	0.84	0.06	0.85		0.84	0.14
Al^{VI}	1.56	0.03	1.72	0.15	2.39	0.08	1.54	0.09	1.74		1.59	0.19
Fe^{2+}	1.54	0.22	1.30	0.05	0.78	0.04	2.57	0.52	2.06		2.35	0.20
Mn	–	–	–	–	–	–	–	–	–		–	–
Mg	1.72	0.33	1.80	0.19	1.76	0.01	1.22	0.35	1.53		1.40	0.32
Ca	–	–	0.02	0.04	–	–	0.05	0.07	–		–	–
Na	–	–	0.04	0.05	–	–	–	–	–		–	–
K	–	–	–	–	–	–	–	–	–		0.01	0.03
Mg/(Mg + Fe)	0.52	0.08	0.58	0.03	0.70	0.01	0.32	0.11	0.43		0.37	0.07
T (°C)[a]	88	4	93	13	57	17	98	2	80		116	46

Calculations are based on 14 oxygen atoms (anhydrous basis).
[a]Temperatures are calculated using the geothermometer from Bourdelle *et al.* (2013).

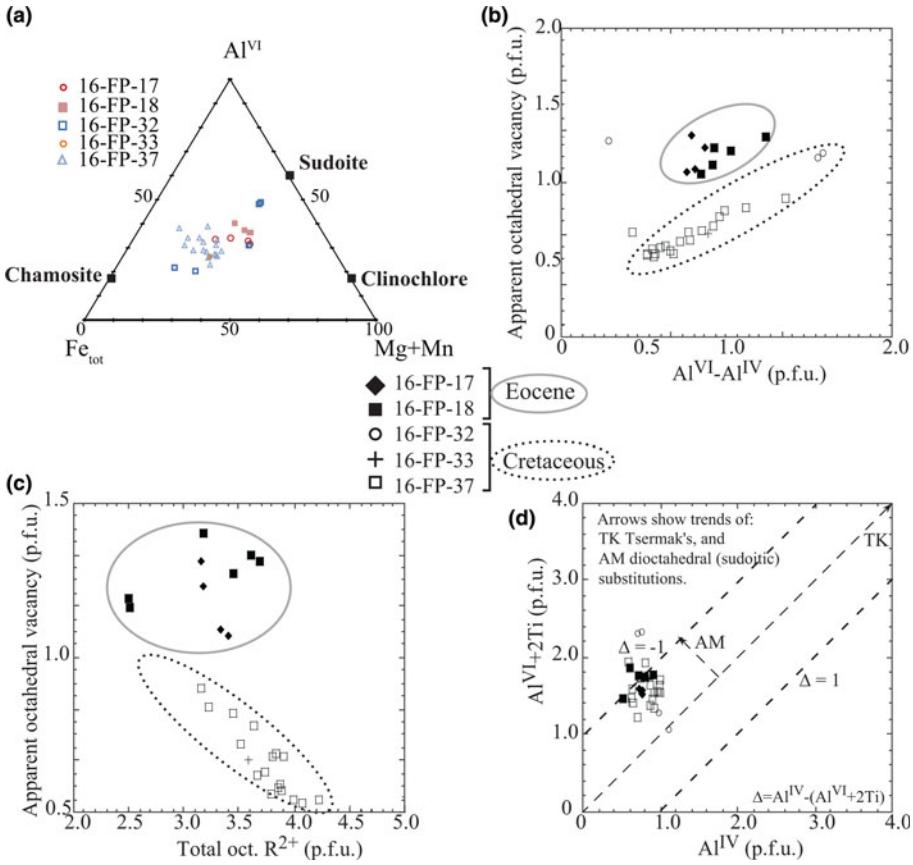

FIG. 9. Compositional variation of chlorite. Cation numbers and ratios are calculated from EDX analyses. (a) Fe_{tot}–(Mg + Mn)–Al^{VI} diagram of chlorite; the end-members chamosite, clinochlore and sudoite are indicated. (b) Apparent octahedral vacancy (= 10−∑octahedral cations p.f.u.) *vs.* Al^{VI} – Al^{IV}. (c) Apparent octahedral vacancy *vs.* total octahedral. R^{2+} (= Fe^{2+} + Mg^{2+}). (d) Al^{VI} + 2Ti *vs.* Al^{IV}. Arrows show trends of Tschermak (TK) and dioctahedral (AM) substitutions, where Δ = Al^{IV} – (Al^{VI} + 2Ti).

temperature ranges (Frey, 1987; Doublier *et al.*, 2012). The temperature estimates for the KI diagenesis–anchizone transition, based on comparison with other geothermometers, range between 180°C and 250°C (Merriman & Frey, 1999; Potel *et al.*, 2006). The VR results (Table 5) and the occurrence of chabazite (Table 2) suggest temperatures below 180°C and 250°C due to the KI values (Table 2).

To better constrain the diagenetic grade, we calculated additional temperatures in the samples using the chlorite geothermometric method of Bourdelle *et al.* (2013). Samples analysed are from the Eocene of the Whakataki fault and from the Cretaceous of the Adams-Tinui fault. The chlorites analysed were selected as neoformed minerals according to their crystal habit. Taking into account the range of standard deviation, including the simplification of assuming Fe to be ferrous (Bourdelle *et al.*, 2013), the estimated temperature was in the range of 80–120°C. These results are compatible with grade of maturity of the organic matter (Table 5) and the temperature stability range of chabazite. Those calculated temperatures show a positive correlation with the KI values of the same samples (Fig. 10b). This pattern seems to reflect a lack of equilibrium of illite-muscovite with chlorite.

Vitrinite reflectance values <1.3 R_r% (±0.15 R_r%) correspond to temperatures of <100°C with a mean temperature uncertainty of ±30°C for various geothermal gradients (Ferreiro Mählmann & Le Bayon, 2016). The VR results of this study vary between 0.85 and 0.96 R_r% for the Adams-Tinui fault and between 0.65

https://doi.org/10.1180/clm.2018.46 Published online by Cambridge University Press

Table 5. VR data for samples inside and outside of the fault zones. Columns 1 and 2: Sample number and ages. Column 3: VR = mean vitrinite reflectance value R_r%. Column 4: *n* = number of measured vitrinite particles. Row 5: standard deviation.

Sample	Age	VR	*n*	SD
Whakataki fault				
16-AK-132	Early Miocene	0.65	51	0.04
16-FP-16	Eocene	0.96	18	0.05
Whareama syncline				
CTU21	Late Miocene	0.55	102	0.07
Tinui fault				
16-FP-26	Late Cretaceous (Whangai)	0.96	12	0.05
16-FP-27	Palaeocene	0.85	9	0.08
16-FP-28	Palaeocene	0.86	12	0.07
16-FP-30	Palaeocene	0.89	7	0.08
16-FP-31	Eocene	–	–	–
Kaiwhata Units				
15-FP-07	Palaeocene	1.30	9	0.09
Glenburn nappe				
15-AK-76	Cretaceous (Glenburn)	1.08	81	0.08
15-FP-06	Cretaceous (Longbush)	1.10	7	0.08

and 0.96 R_r% for the Whakataki fault and reveal low-grade diagenetic zone conditions. Therefore, temperatures might be <100°C in both faults. Temperature estimation using the equation of Bourdelle *et al.* (2013) yielded temperatures between 98°C (±2°C) and 57°C (±17°C). Using the basin maturity chart given by Merriman & Frey (1999) or by Ferreiro Mählmann *et al.* (2012), such values should correlate with KI values >0.60Δ°2θ. Nevertheless, the calculated KI values are <0.60Δ°2θ, except for Early Cretaceous samples of the Adams-Tinui fault (Table 2).

Although all data indicate diagenesis conditions, some differences may be noticed between the various methods. A correlation appears between the temperatures calculated with chlorite geothermometry and the VR values (Fig. 9). However, the KI values do not follow the expected trend. As mentioned before, the KI values are too low, indicating higher temperatures

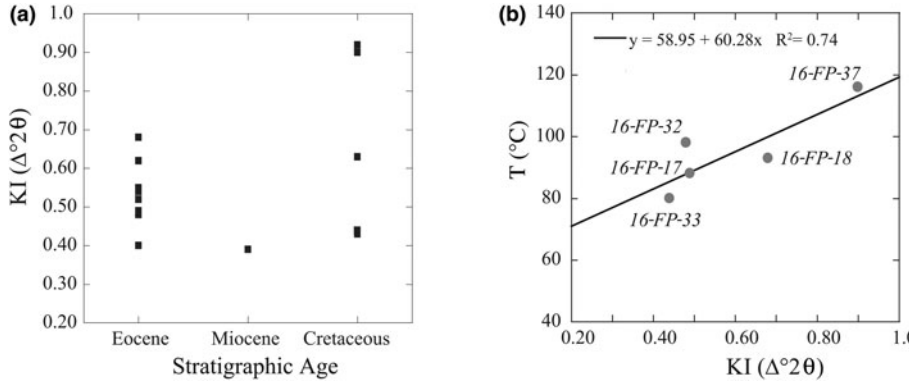

Fig. 10. (a) Correlation between KI values and stratigraphic ages. (b) Correlation between KI values and temperature determined in the same samples using the chlorite geothermometer of Bourdelle *et al.* (2013).

https://doi.org/10.1180/clm.2018.46 Published online by Cambridge University Press

compared to the other analytical methods. In addition, a positive correlation is observed between clay mineral paragenesis, calculated temperature and KI values. Furthermore, the correlation between KI and VR should be negative (see Ferreiro Mählmann *et al.*, 2012, and references therein). Here, the positive slope is the opposite of the relation proposed by Ferreiro Mählmann *et al.* (2012) and Ferreiro Mählmann & Le Bayon (2016) depending on the P–T–t–D (pressure–temperature–time–deformation) history and fluid activity. Only samples from the Early Cretaceous show coherent results for all the indicators used. Various relations correlate with KI indicating higher-grade diagenesis with immature VR and bituminite reflectance (BR) and low temperatures. Using the KI/VR plot of Ferreiro Mählmann & Giger (2012), the KI values 0.39–0.55Δ°2θ of the Whakataki fault (Table 2) fall in the data triangle of correlation values controlled by detrital mica. The presence of detrital minerals was confirmed in thin sections, where sericitic and hydro-biotite detrital flakes, rounded detrital feldspar and some opaque minerals were observed. The <2 μm fraction of samples in formations younger than the Early Cretaceous contain detrital components that are not re-equilibrated (*i.e.* contaminated by detrital clay minerals). Therefore, detailed clay mineralogical work based on the study of variously sized fractions would enable the distinction between detrital components (usually the coarser-grained fraction) and authigenic components (the finest-grained fraction). The neoformation of clay minerals is a slower process than the grain size reduction associated with deformation in the fault zone, causing a reduction in clay 'crystallinity' values (Giorgetti *et al.*, 2000; Abad *et al.*, 2003b). Only in the Early Cretaceous samples has sufficient time elapsed to allow almost complete recrystallization of clay minerals and the establishment of an equilibrium with neoformed minerals. In contrast, the temperature obtained for chlorite is interpreted as resulting from neoformed chlorite in Eocene and Torlesse formations (Early Cretaceous), and is thus contemporaneous to the maturation rank of organic matter. Warr & Cox (2016) outlined that the evolution of clay 'crystallinity' is a function of the activities of K^+, Fe^{2+} and Mg^{2+} in the metamorphic pore fluid. The illitization and eventual muscovite formation are reactions influenced by the reactivity of K^+ (Huang *et al.*, 1993), whereas the chloritization process is more dependent on the reactivity of Mg^{2+} and Fe^{2+} (Jahren & Aagaard, 1989). In the studied area, the activity of K^+ should be low compared with the activities of Mg^{2+} and Fe^{2+}, favouring the formation and growth of neoformed chlorite, whereas growth of illite is slower, enabling the alteration of KI values due to detrital illite.

The KI values are broader than those expected according to the other methods used. The KI measured from most samples might not be related to increasing diagenetic grade. In samples from low-grade diagenetic zones, detrital illite predominates and has influenced the mean of the bulk population measured using the KI. Recrystallization of detrital mica and neoformation of illite are slow and in competition with tectonic strain.

The relationship between KI and VR seems to establish coherently the same diagenetic grade only in the Early Cretaceous samples. These samples experienced long-lasting and deep burial; thus, the reaction progress for illite approached steady-state conditions at peak diagenetic pressures (burial and tectonic load) and temperatures. In younger formations, the low peak burial grade within the subduction wedge did not allow re-equilibration (recrystallization) of illite derived from a source of a higher metamorphic grade in the hinterland, and neoformation of illite did not advance. However, even if illite was not at equilibrium, the effect of physical grinding during tectonic activity might be observed *via* the decrease of KI values close to the main faults (*e.g.* along the Adams-Tinui fault; Fig. 7). A study of various fraction sizes might help to determine the occurrence of inherited illite by determining the IC values of detrital and neoformed clay minerals. This would help to explain the low KI values observed in the samples. This phenomenon might also hold for kaolinite 'crystallinity' (Fig. 7).

A strong correlation exists between the temperatures determined by chlorite geothermometry and temperatures deduced from VR values. No variation was observed in the fault zones; the higher temperatures were observed in the older formation (Table 4, Fig. 7). In chlorites, the activities of K^+, Mg^{2+} and Fe^{2+} might play a role in the neoformation and re-equilibration of clays (Warr & Cox, 2016). In the Hikurangi prism, the chlorite geothermometer of Bourdelle *et al.* (2013) provides more reliable temperature measures than the temperatures estimated *via* KI values. The occurrence of kaolinite in the samples confirms the diagenetic grade. The disappearance of kaolinite occurs before the diagenetic zone–anchizone boundary due to illitization and chloritization, unless the environment is Al-rich. However, it may persist in carbonate rocks, sedimentary rocks rich in organic matter or volcaniclastic rocks with R_r values of 1.3 ± 0.15% (Kisch, 1987; Ferreiro Mählmann, 2001). Kaolinitization of detrital plagioclase, orthoclase and mica in a Ca-rich environment

https://doi.org/10.1180/clm.2018.46 Published online by Cambridge University Press

enhanced by de-carbonatization of plagioclase and illitization (sericitization) of K/Na-feldspars leads to significant potential for the kaolinite formation that is typical in low-grade diagenesis, which progressively disappears in high-grade diagenesis. This is compatible with the migration of oil observed in the rocks in the oil-window (mature zone).

CONCLUSION

The low-grade diagenetic gradual evolution of clay minerals and the maturity of organic matter in the Whakataki and Adams-Tinui fault zones have been studied, combined with the evolution of the KI and the determination of temperatures using the chlorite geothermometer of Bourdelle *et al.* (2013). The resulting temperatures were compared with *T* (°C)–KI–VR correlations presented in the literature. Various evolutions of the organic and mineralogical parameters were observed in the fault zones.

It was shown that:

(1) The thermal burial grade is of the high-grade diagenetic zone (KI = 1.0 ± 0.15Δ°2θ), corresponding to VR = 1.3 ± 0.15% (high-volatility bituminous/medium-volatility bituminous coal), with a temperature of ∼100°C.
(2) The physical grinding of minerals during tectonic activity with increases of deformation close to the fault, where tectonic strain proceeds faster than recrystallization, reduced phyllosilicate crystal size, thereby reducing clay 'crystallinity' values for illite and kaolinite.
(3) Burial time was important for the equilibrium of clays (chemical and structural homogeneity) in the low-grade diagenetic zone, where inherited structures and the chemistry of detrital phases predominated, specifically in subduction wedges.
(4) Rocks from a subduction wedge in close proximity to a metasedimentary hinterland are inappropriate for the sampling and use of KI to determine grade of diagenesis if there exists little difference between the sediments and their source.

ACKNOWLEDGEMENTS

UniLaSalle Beauvais is thanked for its financial support of the PhD thesis of P. Malié (2014–2017) on the project. The manuscript has benefited greatly from thoughtful review from two anonymous reviewers. A. Schleicher and G. Christidis are also thanked for their management as editors of the article.

REFERENCES

Abad I., Gutiérrez-Alonso G., Nieto F., Gertner I., Becker A. & Cabero A. (2003a) The structure and the phyllosilicates (chemistry, crystallinity and texture) of Talas Ala-Tau (Tien Shan, Kyrgyz Republic): comparison with more recent subduction complexes. *Tectonophysics*, **365**, 103–127.

Abad I., Nieto F. & Gutiérrez-Alonso G. (2003b) Textural and chemical changes in slate-forming phyllosilicates across the external-internal zones transition in the low-grade metamorphic belt of the NW Iberian Variscan Chain. *Schweizerische Mineralogische und Petrographische Mitteilungen*, **83**, 63–80.

Abd Elmola A., Charpentier D., Buatier M., Lanari P. & Monié P. (2017) Textural–chemical changes and deformation conditions registered by phyllosilicates in fault zone (Pic de Port Vieux thrust, Pyrenees). *Applied Clay Science*, **144**, 88–103.

Allen P.A. & Allen J.R. (2005) *Basin Analysis: Principles and Applications*. Blackwell, New York, NY, USA.

Aparicio P. & Galán E. (1999) Mineralogical interference on kaolinite crystallinity index measurements. *Clays and Clay Minerals*, **47**, 12–27.

Árkai P. (1991) Chlorite crystallinity: an empirical approach and correlation with illite crystallinity, coal rank and mineral facies as exemplified by Palaeozoic and Mesozoic rocks of northeast Hungary. *Journal of Metamorphic Geology*, **9**, 723–734.

Árkai P., Sassi F.P. & Sassi R. (1995) Simultaneous measurements of chlorite and illite crystallinity: a more reliable tool for monitoring low- to very low grade metamorphisms in metapelites. A case study from the Southern Alps (NE Italy). *European Journal of Mineralogy*, **7**, 1115–1128.

Árkai P., Ferreiro Mählmann R., Suchy V., Balogh K., Sýkorová I. & Frey M. (2002) Possible effects of tectonic shear strain on phyllosilicates: a case study from the Kandersteg area, Helvetic domain, Central Alps, Switzerland. *Schweizerische Mineralogische und Petrographische Mitteilungen*, **82**, 273–290.

Árkai P., Faryad S.W., Vidal O. & Balogh K. (2003) Very low-grade metamorphism of sedimentary rocks of the Meliata unit, Western Carpathians, Slovakia: implications of phyllosilicate characteristics. *International Journal of Earth Sciences*, **92**, 68–85.

Árkai P., Sassi F.P. & Desmons J. (2007) Very low- to low-grade metamorphic rocks. Pp. 36–42 in: *Metamorphic Rocks: A Classification and Glossary of Terms: Recommendations of the International Union of Geological Sciences Subcommission on the Systematics of Metamorphic Rocks* (D. Fettes & J.

https://doi.org/10.1180/clm.2018.46 Published online by Cambridge University Press

Desmons, editors). Cambridge University Press, Cambridge, UK.

Bailleul J., Chanier F., Ferrière J., Robin C., Nicol A., Mahieux G., Gorini C. & Caron V. (2013) Neogene evolution of lower trench-slope basins and wedge development in the central Hikurangi subduction margin, New Zealand. *Tectonophysics*, **591**, 152–174.

Bangs N.L., Shipley T.H., Moore J.C. & Moore G.F. (1999) Fluid accumulation and channeling along the northern Barbados décollement thrust. *Journal of Geophysical Research*, **104**, 399–414.

Barnes P.M., Lamarche G., Bialas J., Henrys S., Pecher I., Netzeband G.L., Greinert J., Mountjoy J.J., Pedley K. & Crutchley G. (2010) Tectonic and geological framework for gas hydrates and cold seeps on the Hikurangi subduction margin, New Zealand. *Marine Geology*, **272**, 26–48.

Barrow G. (1893) On an intrusion of muscovite–biotite gneiss in the south-eastern Highlands of Scotland and it accompanying metamorphism. *Journal of the Geological Society*, **49**, 330–358.

Bourdelle F., Parra T., Chopin C. & Beyssac O. (2013) A new chlorite geothermometers for diagenetic to low-grade metamorphic conditions. *Contributions to Mineralogy and Petrology*, **165**, 723–735.

Bruhn R., Parry W. & Bunds M. (2000) Tectonics, fluid migration, and fluid pressure in a deformed forearc basin, Cook Inlet, Alaska. *Geological Society of America Bulletin*, **112**, 550–563.

Buatier M.D., Chauvet A., Kanitpanyacharoen W., Wenk H.R., Ritz J.F. & Jolivet M. (2012) Origin and behavior of clay minerals in the Bogd fault gouge, Mongolia. *Journal of Structural Geology*, **34**, 77–90.

Buatier M.D., Cavailhes T., Charpentier D., Lerat J., Sizun J.P., Labaume P. & Gout C. (2015) Evidence of multi-stage faulting by clay mineral analysis: example in a normal fault zone affecting arkosic sandstones (Annot sandstones). *Journal of Structural Geology*, **75**, 101–117.

Chandra D. (1965) Reflectance of coals carbonized under pressure. *Economic Geology*, **60**, 621–629.

Chanier F. (1990) Mud volcanoes on the emerged ridge of the Hikurangi accretionary prism, New Zealand; tectonic setting and structural signification. P. 99 in: *Book of Abstracts*, International Conference on Fluids in Subduction Zones and Related Processes, Paris, 1990.

Chanier F. (1991) *Le Prisme d'Accrétion Hikurangi: Un Témoin de l'Évolution Géodynamique d'une Marge Active Péripacifique (Nouvelle-Zélande)*. Unpublished PhD thesis, Université des Sciences et Techniques de Lille-Flandres-Artois, Villeneuve d'Ascq, France.

Chanier F. & Ferrière J. (1989) Sur l'existence de mouvements tangentiels majeurs dans la chaîne côtière orientale de Nouvelle Zélande; signification dans le cadre de la subduction de la plaque Pacifique. *Comptes Rendus de l'Académie des Sciences* (*Paris*), **308**, 1645–1650.

Chanier F. & Ferrière J. (1991) From a passive to an active margin: tectonic and sedimentary processes linked to the birth of an accretionary prism (Hikurangi Margin, New Zealand). *Bulletin de la Société Géologique de France*, **162**, 649–660.

Chanier F., Ferrière J. & Angelier J. (1992) Extension et érosion tectonique dans un prisme d'accrétion: l'exemple du Prisme Hikurangi (Nouvelle-Zélande). *Comptes Rendus de l'Académie des Sciences* (*Paris*), **315**, 741–747.

Chanier F., Ferrière J. & Angelier J. (1999) Extensional deformation across an active margin, relations with subsidence, uplift and rotations: the Hikurangi subduction, New Zealand. *Tectonics*, **18**, 862–876.

Crutchley G.J., Pecher I.A., Gorman A.R., Henrys S.A. & Greinert J. (2010) Seismic imaging of gas conduits beneath seafloor seep sites in a shallow marine gas hydrate province, Hikurangi Margin, New Zealand. *Marine Geology*, **272**, 114–126.

Dalla Torre M., Livi K.J.T. & Frey M. (1996) Chlorites textures and composition from high pressure/low temperature metashales and metagraywackes, Franciscan complex, Diablo Range, California, U.S.A. *European Journal of Mineralogy*, **8**, 825–846.

Dalla Torre M., Ferreiro Mählmann R. & Ernst W.G. (1997) Experimental study on the pressure dependence of vitrinite maturation. *Geochimica et Cosmochimica Acta*, **61**, 2921–2928.

Deer W.A., Howie R.A. & Zussman J. (2013) *An Introduction to the Rock-Forming Minerals*, 3rd edition. Mineralogical Society, London, UK.

Delteil J., Morgans H.E.G., Raine J.I., Field B.D. & Cutten H.N.C. (1996) Early Miocene thin-skinned tectonics and wrench faulting in the Pongaroa district, Hikurangi margin, North Island, New Zealand. *New Zealand Journal of Geology and Geophysics*, **39**, 271–282.

Doublier M.P, Roache T., Potel S. & Laukamp C. (2012) Short-wavelength infrared spectroscopy of chlorite can be used to determine very low metamorphic grades. *European Journal of Mineralogy*, **24**, 891–902.

Ferreiro Mählmann R. (2001) Correlation of very low grade data to calibrate a thermal maturity model in a nappe tectonic setting, a case study from the Alps. *Tectonophysics*, **334**, 1–33.

Ferreiro Mählmann R. & Frey M. (2012) Standardisation, calibration and correlation of the Kübler-index and the vitrinite/bituminite reflectance: an inter-laboratory and field related study. *Swiss Journal of Geosciences*, **105**, 153–170.

Ferreiro Mählmann R. & Giger M. (2012) The Arosa zone in Eastern Switzerland: oceanic, sedimentary burial, accretional and orogenic very low-to low grade patterns in a tectono-metamorphic mélange. *Swiss Journal of Geosciences*, **105**, 203–233.

Ferreiro Mählmann R. & Le Bayon R. (2016) Vitrinite and vitrinite like solid bitumen reflectance in thermal

https://doi.org/10.1180/clm.2018.46 Published online by Cambridge University Press

maturity studies: correlations from diagenesis to incipient metamorphism in different geodynamic settings. *International Journal of Coal Geology*, **157**, 52–73.

Ferreiro Mählmann R., Botzkaya O., Potel S., Le Bayon R., Šegvić B. & Nieto García F. (2012) The pioneer work of Bernard Kübler and Martin Frey in very low-grade metamorphic terranes: paleo-geothermal potential of variation in Kübler-Index/organic matter reflectance correlations. A review. *Swiss Journal of Geosciences*, **105**, 121–152.

Field B.D., Uruski C.I. & Institute of Geological and Nuclear Sciences Limited (1997) *Cretaceous–Cenozoic Geology and Petroleum Systems of the East Coast Region, New Zealand*. Institute of Geological and Nuclear Sciences, Lower Hutt, New Zealand.

Frey M. (1987) *Low Temperature Metamorphism*. Blackie, Glasgow and London, UK.

George A.D. (1990) Deformation processes in an accretionary prism: a study from the Torlesse terrane of New Zealand. *Journal of Structural Geology*, **12**, 747–759.

George A.D. (1992) Deposition and deformation of an Early Cretaceous trench-slope basin deposit, Torlesse terrane, New Zealand. *Geological Society of America Bulletin*, **104**, 570–580.

Giorgetti G., Memmi I. & Peacor D. (2000) Retarded illite crystallinity caused by stress-induced sub-grain boundaries in illite. *Clay Minerals*, **35**, 693–708.

Guggenheim S., Bain D.C., Bergaya F., Brigatti M.F., Drits V., Eberl D.D., Formoso M., Galán E., Merriman R.J., Peacor D.R., Stanjek H. & Watanabe T. (2002) Report of the AIPEA nomenclature committee for 2001: order, disorder and crystallinity in phyllosilicates and the use of the 'crystallinity index'. *Clay Minerals*, **37**, 389–393.

Guidotti C.V., Sassi F.P. & Blencoe J.G. (1989) Compositional controls on the a and b cell dimensions of 2*M*1 muscovites. *European Journal of Mineralogy*, **1**, 71–84.

Henry P., Lallemant S., Nakamura K., Tsunogai U., Mazzotti S. & Kobayashi K. (2002) Surface expression of fluid venting at the toe of the Nankai wedge and implications for flow paths. *Marine Geology*, **187**, 119–143.

Henrys S.A., Woodward D. & Pecher I.A. (2009) Variation of bottom-simulating-reflection strength in a high-flux methane province, Hikurangi margin, New Zealand. *AAPG Memoir*, **89**, 481–489.

Hollis C.J., Tayler M., Andrew B., Taylor K., Lurcock P., Bul P., Kulhanek D. *et al.* (2014) Organic-rich sedimentation in the South Pacific Ocean associated with Late Paleocene climatic cooling. *Earth-Science Reviews*, **134**, 81–97.

Huang W.L., Longo J.M. & Pevear D.R. (1993) An experimentally derived kinetic model for smectite-to-illite conversion and its use as a geothermometer. *Clays and Clay Minerals*, **41**, 162–162.

Jahren J.S. & Aagaard P. (1989) Compositional variations in diagenetic chlorites and illites, and relationships with formation-water chemistry. *Clay Minerals*, **24**, 157–170.

Kisch H.J. (1987) Correlation between indicators of very low grade metamorphism. Pp. 227–300 in: *Low Temperature Metamorphism* (M. Frey, editor). Blackie, Glasgow & London, UK.

Kisch H.J. (1991) Illite crystallinity: recommendation on sample preparation, X-ray diffraction settings, and interlaboratory samples. *Journal of Metamorphic Geology*, **9**, 665–670.

Kretz R. (1983) Symbols for rock-forming minerals. *American Mineralogist*, **68**, 277–279.

Kübler B. (1964) Les argiles, indicateurs de métamorphisme. *Revue de l'Institut Français du Pétrole*, **19**, 1093–1112.

Kübler B. (1967) La cristallinité de l'illite et les zones tout à fait supérieures du métamorphisme. Pp. 105–122 in: *Etages Tectoniques*. Baconnière, Neuchâtel, Switzerland.

Kübler B., Betrixe M.A. & Monnier F. (1979) Les premiers stades de la diagenèse organique et la diagenèse minérale: une tentative d'équivalence. 1ère partie: zonéographie par la maturation de la matière organique. *Bulletin der Vereinigung Schweizerischer Petroleumgeologen und Petroleumingenieure*, **45**, 1–22.

Lacroix B., Charpentier D., Buatier M., Vennemann T., Labaume P., Adatte T., Travé A. & Dubois M. (2012) Formation of chlorite during thrust fault reactivation. Record of fluid origin and P–T conditions in the Monte Perdido thrust fault (southern Pyrenees). *Contributions to Mineralogy and Petrology*, **163**, 1083–1102.

Le Bayon R., Brey G.P., Ernst W.G. & Ferreiro Mählmann R. (2011) Experimental kinetic study of organic matter maturation: time and pressure effects on vitrinite reflectance at 400°C. *Organic Geochemistry*, **42**, 340–355.

Le Pichon X., Henry P. & Lallemand S. (1990) Water flow in the Barbados accretionary complex. *Journal of Geophysical Research*, **95**, 8945–8968.

Lee J.M. & Begg J.G. (2002) *Geology of the Wairarapa Area. Institute of Geological and Nuclear Sciences, 1:250,000 Geological Map 11*. Institute of Geological and Nuclear Sciences, Lower Hutt, New Zealand.

Lewis K.B. & Marshall B.A. (1996) Seep faunas and other indicators of methane-rich dewatering on the New Zealand convergent margins. *New Zealand Journal of Geology and Geophysics*, **39**, 181–200.

Lewis K. & Pettinga J.R. (1993) The emerging, imbricate frontal wedge of the Hikurangi margin. *Sedimentary Basins of the World*, **2**, 225–250.

Merriman R.J. & Frey M. (1999) Patterns of very low-grade metamorphism in metapelitic rocks. Pp. 61–107

https://doi.org/10.1180/clm.2018.46 Published online by Cambridge University Press

in: *Low-Grade Metamorphism* (M. Frey & D. Robinson, editors). Blackwell Science, Oxford, UK.

Merriman R.J., Roberts B. & Peacor D.R. (1990) A transmission electron microscope study of white mica crystallite size distribution in a mudstone to slate transitional sequence, North Wales, UK. *Contributions to Mineralogy and Petrology*, **106**, 27–40.

Moore G.F., Shipley T.H., Stoffa P.L., Karig D.E., Taira A., Kuramoto S., Tokuyama H. & Suyehiro K. (1990) Structure of the Nankai Trough accretionary zone from multichannel seismic reflection data. *Journal of Geophysical Research*, **95**, 8753–8765.

Moore J.C. & Vrolijk P. (1992) Fluids in accretionary prisms. *Reviews of Geophysics*, **30**, 113–135.

Moore J.C., Moore G.F., Cochrane G.R. & Tobin H.J. (1995) Negative-polarity seismic reflections along faults of the Oregon accretionary prism: indicators of overpressuring. *Journal of Geophysical Research*, **100**, 12895–12906.

Moore P.R. (1988) *Structural Divisions of Eastern North Island, New Zealand*. New Zealand Geological Survey, Wellington, New Zealand.

Mullis J., Ferreiro Mählmann R.F. & Wolf M. (2017) Fluid inclusion microthermometry to calibrate vitrinite reflectance (between 50 and 270°C), illite Kübler-index data and the diagenesis/anchizone boundary in the external part of the Central Alps. *Applied Clay Science*, **143**, 307–319.

Nicol A. & Beavan J. (2003) Shortening of an overriding plate and its implications for slip on a subduction thrust, central Hikurangi Margin, New Zealand. *Tectonics*, **22**, 1070.

Nicol A., Van Dissen R., Vella P., Alloway B. & Melhuish A. (2002) Growth of contractional structures during the last 10 m.y. at the southern end of the emergent Hikurangi forearc basin, New Zealand. *New Zealand Journal of Geology and Geophysics*, **45**, 365–385.

Nicol A., Mazengarb C., Chanier F., Rait G., Uruski C. & Wallace L. (2007) Tectonic evolution of the active Hikurangi subduction margin, New Zealand, since the Oligocene. *Tectonics*, **26**, TC4002.

Pecher I.A., Henrys S.A., Wood W.T., Kukowski N., Crutchley G.J., Fohrmann M., Kilner J., Senger K., Gorman A.R. & Coffin R.B. (2010) Focussed fluid flow on the Hikurangi Margin, New Zealand – evidence from possible local upwarping of the base of gas hydrate stability. *Marine Geology*, **272**, 99–113.

Plaza-Faverola A., Klaeschen D., Barnes P., Pecher I., Henrys S. & Mountjoy J. (2012) Evolution of fluid expulsion and controls on hydrate formation across the southern Hikurangi subduction Margin, New Zealand. *Geochemistry Geophysics Geosystems*, **13**, Q08018.

Plaza-Faverola A., Pecher I., Crutchley G., Barnes P., Bünz S., Golding T., Klaeschen D., Papenberg C. & Bialas J. (2014) Submarine gas seepage in a mixed contractional and shear deformation regime: cases from the Hikurangi oblique–subduction margin. *Geochemistry Geophysics Geosystems*, **15**, 416–433.

Polissar P.J., Savage H.M. & Brodsky E.E. (2011) Extractable organic material in fault zones as a tool to investigate frictional stress. *Earth and Planetary Science Letters*, **311**, 439–447.

Potel S., Ferreiro Mählmann R., Stern W.B., Mullis J. & Frey M. (2006) Very low-grade metamorphic evolution of pelitic rocks under high-pressure/low-temperature conditions, NW New Caledonia (SW Pacific). *Journal of Petrology*, **47**, 991–1015.

Potel S., Maison T., Maillet M., Sarr A.C., Doublier M .P., Trullenque G & Ferreiro Mählmann R. (2016) Reliability of very low-grade metamorphic methods to decipher basin evolution: case study from the Markstein basin (southern Vosges, NE France). *Applied Clay Science*, **134**, 175–185.

Rait G.J., Chanier F. & Waters D.W. (1991) Landward and seaward directed thrusting accompanying the onset of subduction beneath New Zealand. *Geology*, **19**, 230–233.

Schleicher A.M., Sutherland R., Townend J., Toy V.G. & van der Pluijm B.A. (2015) Clay mineral formation and fabric development in the DFDP-1B borehole, central Alpine fault, New Zealand. *New Zealand Journal of Geology and Geophysics*, **58**, 13–21.

Schmidt D., Schmidt S.T., Mullis J., Ferreiro Mählmann R. & Frey M. (1997) Very low grade metamorphism of the Taveyanne formation of western Switzerland. *Contributions to Mineralogy and Petrology*, **129**, 385–403.

Sibson R.H. & Rowland J.V. (2003) Stress, fluid pressure, and structural permeability in seismogenic crust, North Island, New Zealand. *Geophysical Journal International*, **154**, 584–594.

Suneson N.H. (1993) The geology of the Torlesse Complex along the Wellington area coast, North Island, New Zealand. *New Zealand Journal of Geology and Geophysics*, **36**, 369–384.

Taylor G.H., Teichmüller M., Davies A., Diessel C.F.K., Littke R. & Robert P. (1998) *Organic Petrology*. Gebrüder Borntraeger, Berlin, Germany.

Tilley C.E. (1925) Metamorphic zones in the southern Highlands of Scotland. *Journal of Geological Society*, **81**, 100–112.

Trincal V., Charpentier D., Buatier M.D., Grobety B., Lacroix B., Labaume P. & Sizun J.P. (2014) Quantification of mass transfers and mineralogical transformations in a thrust fault (Monte Perdido thrust unit, southern Pyrenees, Spain). *Marine and Petroleum Geology*, **55**, 160–175.

Warr L.N. & Rice A.H. (1994) Interlaboratory standardization and calibration of clay mineral crystallinity and crystallite size data. *Journal of Metamorphic Geology*, **12**, 141–152.

Warr L.N. & Ferreiro Mählmann R. (2015) Recommendations for Kübler index standardization. *Clay Minerals*, **50**, 282–285.

https://doi.org/10.1180/clm.2018.46 Published online by Cambridge University Press

Warr L.N. & Cox S.C. (2016) Correlating illite (Kübler) and chlorite (Árkai) 'crystallinity' indices with metamorphic mineral zones of the South Island, New Zealand. *Applied Clay Science*, **134**, 164–174.

Winkler H.G.F. (1979) *Petrogenesis of Metamorphic Rocks*, 5th edition. Springer, Berlin, Germany.

Zane A. & Weiss Z. (1998) A procedure for classifying rock-forming chlorites based on microprobe data. *Rendiconti Lincei Scienze Fisiche e Naturali*, **9**, 51–56.

https://doi.org/10.1180/clm.2018.46 Published online by Cambridge University Press